Analyzing Constellation Performance for the Radio Occultation Tomography of Internal Gravity Waves

Riley Fitzgerald, *Non-member,* Lucy Halperin, *Non-member,* Stephen Leroy, *Non-member,* Amelia Gagnon, *Member, IEEE* Kerri Cahoy, *Member, IEEE* and James Clark, *Non-member, IEEE*

***Abstract*—Radio occultation (RO) is a powerful tool for remotely sensing the atmosphere, producing globally distributed soundings with high vertical resolution and high temperature retrieval accuracy, especially in the stratosphere. The spatial distribution of the soundings typically prevents the use of these measurements for studying atmospheric effects with small horizontal or temporal scales. However, careful arrangement of a dedicated RO constellation can yield sounding clusters useful for the tomographic reconstruction of internal gravity waves with horizontal wavelengths in the tens of kilometers. This paper presents occultation cluster quality metrics predictive of internal gravity wave tomographic reconstruction error and uses these metrics to compare the performance of two alternative RO constellation geometries, mutual orbit groups (MOG) and a spread in right ascension of the ascending node (RAAN). MOG constellations have better overall performance and yield more consistent cluster quality across all sampled latitudes, while RAAN-spread constellations have improved equatorial quality and a trend toward reduced quality at the edges of the latitude range. Additionally, analysis of clusters by latitude, ray azimuth, and quality is performed in order to examine the trends in the outlier best- and worst-performing clusters for each constellation type.**

I. Introduction

INTERNAL gravity waves in atmospheres are waves whose restoring force is buoyancy and that propagate in three dimensions, carrying with them energy and momentum. As opposed to the well-known planetary waves associated with synoptic weather systems—such as barotropic and baroclinic waves—internal gravity waves occur at such small horizontal and vertical scales that they are nearly impossible to probe from space. Their signatures are omnipresent in temperature and winds measured by radiosondes and by aircraft, especially in the stratosphere, but the inability of space-based remote sensing techniques to characterize their three-dimensional spatial (and temporal) structure inhibits the inference of the amount of momentum and energy they transport. Thus, while these waves tantalize atmospheric scientists and are widely thought to play crucial roles in many atmospheric phenomena [1], including the tropical quasi-biennial oscillation [2], [3], the breakdown of jet streams [4], and stratospheric Brewer-Dobson circulation [5], quantifying the fluxes they carry from the troposphere into the stratosphere, especially at small spatial scales, remains a largely unsolved problem [6].

R. Fitzgerald, L. Halperin, A. Gagnon, K. Cahoy, and J. Clark are at the Massachusetts Institute of Technology, Cambridge, MA, 02139 USA. R. Fitzgerald can be reached by email at rmfitz@mit.edu.

S. Leroy is at Atmospheric and Environmental Research, Inc., Lexington, MA, 02421 USA

Manuscript received ???; revised ???.

Radio occultation (RO) using the transmitters of the Global Navigation Satellite Systems (GNSS) [7], [8] offers a unique opportunity to probe the three-dimensional structure of internal gravity waves at these scales. GNSS RO remotely senses the atmosphere by measuring the frequency shifting of the timing signals of the GNSS transmitting satellites induced by refraction in the atmosphere. Because RO recievers measure both the amplitude and phase of the GNSS signals, physical optics retrievals can effectively perform tomography and thus reconstruct the vertical structure of the atmosphere at scales limited by Fraunhofer diffraction. Vertical resolution of retrieved temperature from RO observations can be as small as 60 m [9]. This enables the remote sensing of internal gravity waves with vertical wavelengths too small (less than 12 km) to be observed by high-spectral-resolution infrared nadir measurement [10]–[12].

RO, because it is a limb sounding technique, cannot in general probe the horizontal structure of the waves in a single retrieved temperature profile (though retrieval of some parameters may be possible in special cases, such as at a critical level where the gravity wave spectrum is saturated, that impose additional constraints [13], [14]). However, recent technological developments have enabled high-performance RO on micro-satellite and nano-satellite form factors [15], [16], and this leads to the possibility of close-formation constellations of RO satellites in low-Earth orbit. When formed carefully, such constellations can obtain clusters of atmospheric profiles within very short temporal and small horizontal windows spread in two dimensions horizontally thousands of times daily. The clusters that result can be analyzed by tomography to infer the horizontal wave-vectors of internal gravity waves that are present and hence also the amounts of momentum and energy they transport vertically. This technique of tomography of internal gravity waves using RO has been demonstrated previously [17], [18] with RO missions of opportunity, but those endeavors yielded very few clusters because the RO satellites involved were not configured so as to yield clusters of soundings with regularity.

One type of close-formation constellation is the *mutual orbit group* (MOG) wherein the satellites within a group of satellites appear to orbit each other mutually as they orbit the Earth [19]. This type of constellation is capable of clustering occultations with spread in two horizontal dimensions globally but the differential regression of nodes caused by the Earth's equatorial bulge disperses the satellites because they are in orbits with slightly perturbed inclinations. Large amounts of propulsion on board the satellites can be expended to maintain

the formation, but existing propulsion systems would expend all of their fuel in a matter of weeks to months. A viable mission, on the other hand, should spread RO soundings of the atmosphere within clusters in two horizontal dimensions without expending quantities of propulsion that severely limit the operational lifetime of the mission.

A close-formation constellation of RO satellites that are spread in the right ascension of ascending node (RAAN) without inclination tilting might be able to spread RO atmospheric soundings within clusters in two horizontal dimensions regularly without expending prohibitive quantities of propulsion. Because the satellites would have precisely the same inclination and semi-major axis, their lines of nodes would regress at the same rate (due to the J_2 term in the Earth's gravity field) and therefore remain in close formation. The constellation would be spread only in RAAN and true latitude at a specific epoch; hence it is a *RAAN-spread* constellation. The satellites would be distributed in the forward velocity direction and in the transverse velocity direction perpendicular to the radial when the formation crosses the equator plane, but the satellites would form a "string of pearls" when at maximum or minimum declination. Intuitively, the clusters of atmospheric soundings that are obtained when the satellite constellation is at low absolute declination are expected to be distributed in two horizontal dimensions, but the soundings within clusters are expected to be co-linear in the horizontal when the satellites are near maximum or minimum declination. If the soundings are co-linear, inferring the two-dimensional horizontal wave-vector of internal gravity waves becomes impossible. Thus, a trade-off is anticipated: MOG constellation formations may yield clusters of RO soundings spread in two horizontal dimensions globally with regularity at the cost of large amounts of on-board propulsion, but RAAN-spread constellation formations would yield clusters of RO soundings spread in two horizontal dimensions reliably only at low latitudes but without having to spend large amounts of on-board propulsion. A thorough analysis of this trade-off is the subject matter of this research.

Note that there are many types of nano-satellite constellations that are possible and desirable for well-defined scientific objectives. The constellations that are described herein are well suited to three-dimensional atmospheric tomography at horizontal scales of tens of kilometers by GNSS radio occultation. If two-dimensional tomography (in one vertical and one horizontal dimension) is all that is necessary to accomplish a scientific objective other than internal gravity wave tomography, then "string-of-pearls" constellations—wherein all of the satellites of the constellation occupy the same orbit—should suffice wherein no on-board propulsion would be necessary and little challenge would be encountered in formation flying.

We intend this paper to be one in a sequence of papers on the development and potential performance of a nano-satellite gravity wave observatory and do not pretend to address all the complications such an observatory is anticipated to encounter. Among such anticipated complications is the fact that radio occultation soundings are not purely vertical and are likely to bias estimation of the vertical wavelength of the gravity waves it sees. Secondly, radio occultation is a limb sounding technique and as such a filtering effect will be incurred, one that preferentially senses gravity waves that propagate transverse to the radio occultation ray-path [20]. Even this effect, though, is mitigated because the effective limb path associated with an atmospheric anomaly is understood to be proportional to the square-root of the vertical scale of the anomaly multiplied by the radius of the Earth [7]: small vertical wavelength gravity waves experience less of a limb filtering effect than large vertical scale waves. Thirdly, a major challenge will be estimating the phase of a gravity wave-mode in the vertical given that most gravity waves exhibit no more than one full cycle in the vertical. Previous work has explored methods to determine the phase of a wave in radio occultation soundings [17, e.g.]. All such complications will be addressed in future research. This paper instead focuses on a much more major architectural issue, and that is whether and how a constellation of nano-satellites might be deployed to form a gravity wave observatory with a multi-year operational lifetime at affordable expense with existing technology.

This paper is organized as follows. In Section II, two metrics (q_1 and q_2) are defined that quantify how well spread the RO profiles within clusters are in two dimensions. Both pertain to the ability with which the horizontal wave-vector of internal gravity waves that are present can be inferred. In Section III, the formation of RAAN-spread RO constellations is described. In Section IV, an in-depth analysis of the qualities of the clusters obtained by MOG and RAAN-spread RO constellations is presented, and the underlying structure of these results is explored in Section V. A summary and conclusions are presented in Section VI.

II. Sounding Clusters and Quality Metrics

This section introduces the notion of RO sounding clusters and metrics which characterize their usefulness for tomographic measurement of internal gravity waves.

Internal gravity wave tomography requires frequent clustering of RO soundings, but such clusters do not occur regularly with existing and past RO satellites. Consider the line in space connecting an RO satellite to an occulting GNSS satellite, as pictured in Fig. 1a; the time of the resulting sounding is taken as the instant this line is tangent to the ellipsoid of the Earth (at straight-line tangent altitude of zero), and the location of the sounding is the point of tangency at that time. A set of RO soundings is considered a cluster if they are closely-spaced in both time and location on the surface of the Earth. Such a cluster is useful in the study of phenomena with small spatial and temporal extent, such as internal gravity waves.

To date, only two dedicated RO constellations, COSMIC and COSMIC-2, have been deployed into orbits designed specifically for RO. (Other past and current RO satellites—those of Spire Global, for example—were deployed in orbits of opportunity, except for the Metop satellites in sun-synchronous orbits.) The COSMIC and COSMIC-2 spacecraft are arranged one-per-plane in circular orbits, with planes spaced evenly in RAAN around the Earth; as a result, they are typically thousands of kilometers apart. This necessitates that any occultations of a given GNSS satellite observed

by separate RO satellites in the constellation will result in soundings which are far apart on the ground. The satellites of the GNSS constellations are also typically far apart in their orbits, implying that occultations of separate GNSS satellites observed in quick succession by a given RO satellite will similarly result in widely-spaced soundings. Moreover, the relative locations of the Earth surface and the GNSS constellations evolve significantly before any RO satellite can return for a second occultation with this GNSS satellite. The period of the RO satellite orbits is approximately 90 minutes; over this time the Earth rotates approximately $22.5°$, and the GPS satellites (for example) travel approximately $45°$ in their orbits.

Soundings which are closely-spaced in both location and time are therefore exceptionally rare, resulting from coincidental arrangements where either

1) two separate RO satellites observe occultations with the same GNSS satellite near a point where their orbits intersect,
2) one RO satellite observes the occultation of two separate GNSS satellites near a point where their orbits intersect, or
3) two separate RO satellites each observe an occultation with a separate GNSS satellite such that the ray paths have close points of tangency.

These situations rely on geometric coincidences. Therefore, typical RO constellation geometries cannot be relied upon to produce sounding clusters with any consistency, let alone produce clusters distributed around the Earth. For example, a six-month simulation of COSMIC-2 (using the same methods described in Section IV-B) yields approximately 2.35 million possible occultations. Of these, only 1.28% have two others within 10 minutes and 100 km which use a different receiver; only 0.06% have more than two.

An RO constellation composed of spacecraft in close formation, however, reliably produces clusters; if a constellation is composed of satellites in slightly perturbed orbits, each satellite in the constellation observes the occulation of a given GNSS satellite and produces soundings at slightly perturbed times and locations. A group of m spacecraft flying close to some reference orbit almost always produces a cluster of m soundings at each location where a sounding would be observed by an RO spacecraft in the reference orbit. RO satellite proximity alone guarantees the production of clusters, but the exact spatial arrangement of the soundings on the ground is dependent on the specific geometry of the satellite constellation. For example, a string-of-pearls constellation (some number of satellites following each other closely in the same orbit) tends to produce clusters distributed linearly along the ground. While any single RO sounding profile is sufficient to observe the vertical component of an internal gravity wave present at the sounding location, the horizontal components of the wave-vector must be inferred from a cluster by tomography. In order to quantify the utility of a specific cluster geometry—and thereby constellation arrangement—for the tomographic reconstruction of internal gravity waves, a simple observation model for the horizontal wave vector

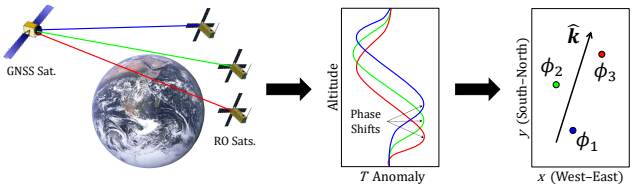

Fig. 1: Outline of the process for internal gravity wave tomography using clustered GNSS RO soundings

component is now introduced and used to derive metrics for cluster quality.

The observation process is outlined in Fig. 1: n GNSS occultations are observed by the RO satellites (Fig. 1a), yielding n closely-spaced soundings; these are approximated to have local two-component Cartesian locations $\boldsymbol{r}_1, \ldots, \boldsymbol{r}_n$ given by points of tangency. In each sounding profile (Fig. 1b), the gravity wave is observed to have phase $\phi_1, \ldots, \phi_n$, respectively. (The process for this phase retrieval is beyond the scope of this work, but will be addressed in future papers.) An estimate of the horizontal component of the wave vector, $\hat{\boldsymbol{k}}$, is then fit to the locations and phases of the soundings in the cluster (Fig. 1c).

The observation model relating these locations $\boldsymbol{r}_i$, phases ϕ_i, and the horizontal component of the wave vector $\boldsymbol{k}$, is given by

$$\phi_i = (\boldsymbol{r}_i - \boldsymbol{r}_0) \cdot \boldsymbol{k} + \phi_0 + \epsilon_i \,, \tag{1}$$

where $\boldsymbol{r}_0$ is a reference location at which the wave has phase ϕ_0, and ϵ_i is the error in the phase observation (assumed to be independent for each i). This model isolates the effects of the horizontal sounding distribution: It assumes that the delay between soundings is small compared to the timescale of the internal gravity wave, and additionally that any 2π ambiguities in wave phase are resolved (which is possible given soundings with sufficiently small phase recovery noise and irrationally-related spacings along the wave vector).

Let the matrix $R \in \mathbb{R}^{n\times 2}$ be constructed such that element R_{ij} gives the x ($j = 1$) or y ($j = 2$) coordinate of sounding i relative to that of $\boldsymbol{r}_0$. Eqn. 1 is written in vector form as $\boldsymbol{\phi} = R\boldsymbol{k} + \phi_0\mathbf{1} + \boldsymbol{\epsilon}$, and the maximum-likelihood estimate of the wave vector is then given by

$$\hat{\boldsymbol{k}} = (R^\mathsf{T}R)^{-1}R^\mathsf{T}(\boldsymbol{\phi} - \phi_0\mathbf{1}) \,. \tag{2}$$

If $\boldsymbol{r}_0$ is taken as the mean location of all soundings $\bar{\boldsymbol{r}} = \frac{1}{n}\sum_{i=1}^{n}\boldsymbol{r}_i$, then $R = \bar{R}$ is given by

$$\bar{R} = \begin{bmatrix} \boldsymbol{r}_1 - \bar{\boldsymbol{r}} & \cdots & \boldsymbol{r}_n - \bar{\boldsymbol{r}} \end{bmatrix}^\mathsf{T} . \tag{3}$$

In this case, Eqn. 2 is independent of the unknown ϕ_0, since by construction $\bar{R}^\mathsf{T}\mathbf{1} = \mathbf{0}$, and the minimum-variance estimate of the horizontal wave vector is obtained. Assuming the errors ϵ_i in the phase observations are independent and have variance σ_ϕ^2, then the error $\hat{\boldsymbol{k}} - \boldsymbol{k}$ of the resulting wave vector estimate has covariance matrix $\sigma_\phi^2(\bar{R}^\mathsf{T}\bar{R})^{-1}$. The uncertainty in the inference of the horizontal wave-vector $\hat{\boldsymbol{k}}$ can be determined

without observations to within a factor of σ_ϕ^2 from only the positions R of the soundings within a cluster.

This covariance forms the basis for two cluster quality metrics, q_1 and q_2:

$$q_1 = \sigma_\phi^2 \left[\det(\bar{R}^\mathsf{T}\bar{R}) \right]^{-1/2} \tag{4a}$$

$$q_2 = \sigma_\phi \left[\lambda_{\min}(\bar{R}^\mathsf{T}\bar{R}) \right]^{-1/2} \tag{4b}$$

Quality metric q_1 represents the total area of uncertainty in wave-vector space, while q_2 represents wave vector uncertainty along the least-certain axis. As such, lower values are desirable for both q_1 and q_2; lower values indicate less uncertainty and more-accurate wave vector reconstruction.

A few properties of RO sounding clusters for utility in internal gravity wave tomography can be inferred from the above definitions:

1) Unique determination of the two-component wave vector and ϕ_0 requires three measurements sampling the same wave (else the rows of $\bar{R}$ become co-linear); for fewer than three soundings, both metrics go to infinity. Estimation of uncertainty (i.e. σ_ϕ) requires over-determination by more than three measurements.
2) As the soundings in a cluster approach colinearity, regardless of their number, these metrics approach infinity. Components of the wave vector perpendicular to the line of soundings cannot be resolved.
3) Both metrics improve as more soundings are added to the cluster.

These properties are demonstrated in the example clusters shown in Fig. 2.

Finally, we note that the phase measurement error σ_ϕ is a property of the system used to make and process the individual observations, not the cluster geometry. The q_1 and q_2 metrics will only be used to study the relative quality of cluster geometries, so $\sigma_\phi = 1$ radian is assumed for the remainder of the paper; this value is conservative, but not unreasonably so. Calculating the exact value will be the subject of future study.

Using the q_1 and q_2 metrics to quantify the quality of individual sounding clusters, we can now examine the ability of different close-flying constellation geometries to reliably produce clusters which are useful for the tomographic reconstruction of internal gravity waves.

III. Constellation Geometries

A carefully designed formation of RO satellites is required in order to optimize the utility of the RO sounding clusters according to the metrics q_1 and q_2. All considered constellations begin with a reference circular orbit with semi-major axis (SMA) a_0, inclination i_0, right-ascension of the ascending node (RAAN) Ω_0, and argument of latitude $u_0 = \omega_0 + M_0$ (the sum of argument of perigee and mean anomaly). This paper will compare the performance of two different RO tomography constellation types which can be defined by small changes to this orbit, (1) Mutual Orbit Group (MOG) constellations and (2) RAAN-spread constellations. These are illustrated qualitatively in Fig. 3.

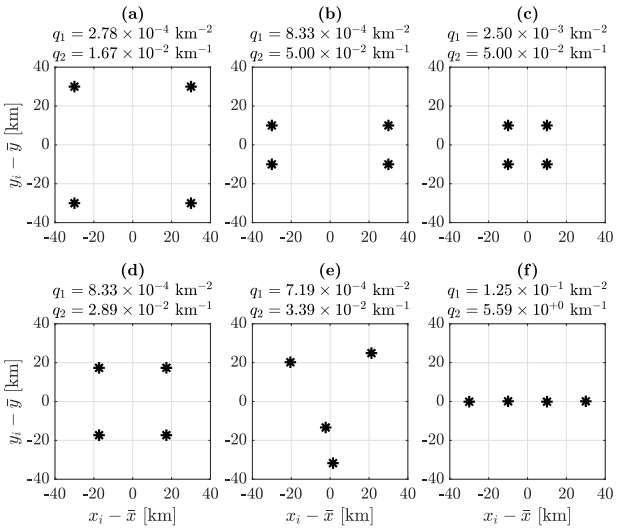

Fig. 2: Example four-sounding clusters and their metric values: (a) is spread evenly in both dimensions; (b) exhibits worse performance than (a) by both metrics; (c) has even worse q_1 than (b) due to reduced overall spread, but equivalent q_2 since the smallest dimension is the same; (d) has the same q_1 as (b), but with improved q_2 due to the more-even spread; (e) is approximately comparable to (d), but with an asymmetric geometry; (f) is nearly co-linear, and exhibits poor performance by both metrics.

A. Mutual orbit group constellations

These constellations are comprised of a series of g mutual orbit groups, or MOGs. Each MOG consists of m satellites that, once per orbit, complete a revolution in relative position to a virtual spacecraft in the reference orbit. This is accomplished by matching all spacecraft mean motions, evenly spacing the orbit angular momentum vectors on a cone of angle δ about the reference angular momentum, and giving each a small eccentricity to extend their relative trajectory in the orbital velocity direction. Each MOG is delayed by time τ in its orbit relative to the previous group. Such a constellation will be referred to as a g-m-τ MOG constellation, with τ specified in seconds. Figure 3a qualitatively shows a MOG constellation, with each satellite in a two-satellite group revolving around a reference orbit as the group travels around the planet.

The MOG arrangement achieves consistent horizontal spacing of satellites in each group, but requires the spacecraft to have slightly different inclinations. As a consequence, each orbit has a slightly different rate of nodal regression due to the J_2 gravitational perturbation, and the constellation requires frequent correction maneuvers (requiring velocity change, or ΔV, on the order of 2–3 $\mathrm{m\,s^{-1}\,day^{-1}}$ in low-Earth orbit). For further discussion of these constellations, their construction, and their maintenance requirements, see [19].

B. RAAN-spread constellations

RAAN-spread constellations are introduced here as an alternative to MOG constellations. A RAAN-spread group also

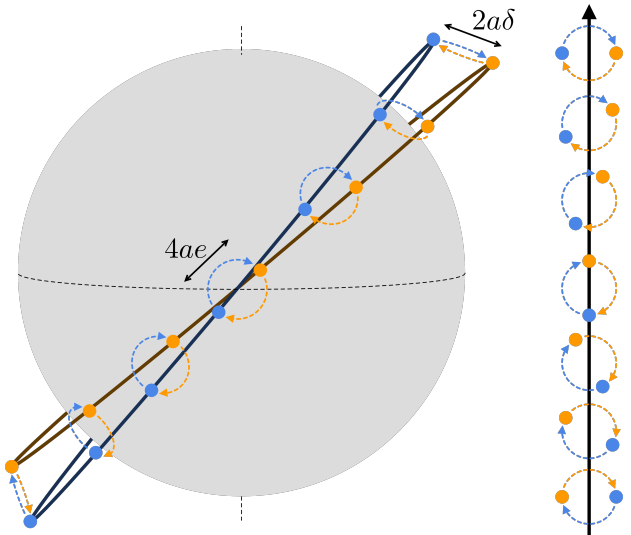

(a) Mutual Orbit Groups

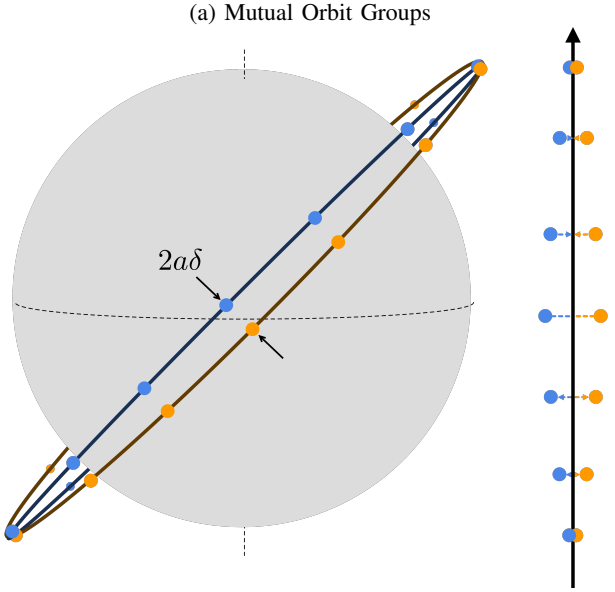

(b) RAAN-spread

Fig. 3: Illustration of two constellation types. a and e are the semi-major axis and eccentricity of the orbits, respectively, and δ is the width parameter of the constellation. The arrow diagrams on the right illustrate the apparent relative motion as the satellite groups move along their reference orbit tracks.

consists of g sub-groups of m spacecraft with orbits close to a circular reference, with each group delayed relative to the previous. Each satellite $(j,k) \in \{1,\dots,g\} \times \{1,\dots,m\}$ has orbital elements given by

$$a_{j,k} = a_0 \tag{5a}$$

$$e_{j,k} = 0 \tag{5b}$$

$$i_{j,k} = i_0 \tag{5c}$$

$$\Omega_{j,k} = \begin{cases} \Omega_0 & m = 1 \\ \Omega_0 + \left(\frac{2k-m-1}{m-1}\right) \sin^{-1}\left(\frac{\sin\delta}{\sin i_0}\right) & m > 1 \end{cases} \tag{5d}$$

$$u_{j,k} = u_0 - \tau(j-1)\sqrt{\mu a_0^{-3}} - \tan^{-1}\left[\cos i_0 \tan(\Omega_{j,k} - \Omega_0)\right] \tag{5e}$$

where μ is the standard gravitational parameter of the Earth. The final terms in Eqns. 5d and 5e are derived from spherical trigonometry, and assure that the spacecraft in each sub-group are exactly abreast with angular separation δ when the group crosses the ascending node. As for MOG constellations, the width parameter δ gives the maximum cross-track angular separation between the spacecraft and the reference orbit, and the delay parameter τ gives the time delay between successive groups passing over the same point in the orbit. Such a constellation will be referred to as a g-m-τ RAAN-spread constellation, again with τ specified in seconds. Figure 3b qualitatively shows a RAAN-spread constellation, with a two-satellite group moving back and forth as it travels around the planet.

RAAN-spread constellations have the advantage of not requiring any spacing of the satellites in inclination, and therefore they do not experience significant differential regression effects. However, they do not offer consistent cross-track spacecraft spacing throughout the orbit, while MOG constellations do. Each group only attains cross-track separation δ at the ascending and descending nodes, and the constellation asymptotes to a string-of-pearls at the maximum and minimum declination out of the equatorial plane. This paper seeks to compare the tomographic performance trade-off between these two constellation types using the introduced quality metrics q_1 and q_2.

IV. Summary of Clusters and Quality Metrics

In this section, the quality of the clusters produced by 26 constellations—13 MOG constellations and 13 corresponding RAAN-spread constellations—is assessed using metrics q_1 and q_2.

A. Considered constellations

The constellation arrangements considered here are listed in the first column of Table I. Each is specified by a three-number series g-m-τ, where g represents the number of groups in the constellation, m represents the number of satellites within each group, and τ represents the time delay between groups, measured in seconds. (For instance, MOG constellation 2-3-60 specifies two MOGs of three satellites each, with a 60-second time delay between each MOG.) For all constellations, the reference inclination and semi-major axis are taken as those of the International Space Station, $i_0 = 51.4°$ and $a_0 = 6778\,\mathrm{km}$, respectively. Additionally, the width parameter δ is taken as $0.174°$, corresponding to a group width of approximately $40\,\mathrm{km}$. This width was chosen to approximately match the horizontal wavelength of the internal gravity waves we seek to probe.

The need for significant constellation maintenance using on-board propulsion disfavors MOG constellations; the ΔV required to counteract differential nodal regression for the MOG constellations is 2–3 $\mathrm{m\,s^{-1}\,day^{-1}}$ [19], which is not required for the RAAN-spread constellations. Other maintenance tasks, for example phasing and altitude maintenence to counteract atmospheric drag effects, should depend mostly on the reference

TABLE I: Mean, min., and max. ΔV required to deploy the satellites of each MOG and RAAN-spread (RS) constellation from ISS orbit. g-m-τ specifies g groups with m satellites each, and a τ-second along-track delay between each group.

Constel.	MOG Dep. ΔV [m/s]			RS Dep. ΔV [m/s]		
g-m-τ [s]	Mean	Min.	Max.	Mean	Min.	Max.
2-2-60	63.0	55.8	70.2	53.0	52.9	53.0
2-2-150	63.1	56.1	70.2	53.1	52.9	53.3
2-2-300	63.4	56.6	70.2	53.3	52.9	53.8
2-2-600	63.8	57.5	70.2	53.8	52.9	54.7
3-3-60	94.5	70.2	108.3	35.4	0.0	53.2
3-3-150	94.8	70.2	108.8	35.7	0.0	53.8
3-3-300	95.2	70.2	109.8	36.2	0.0	54.7
3-3-600	96.2	70.2	111.6	37.1	0.0	56.6
2-3-60	92.4	70.2	103.6	35.3	0.0	53.0
2-3-150	92.5	70.2	103.8	35.5	0.0	53.3
2-3-300	92.8	70.2	104.3	35.7	0.0	53.8
2-3-600	93.2	70.2	105.2	36.2	0.0	54.7
3-4-600	87.0	55.6	107.4	54.7	52.9	56.6

orbit, and therefore require comparable ΔV for all considered constellations. The mean, minimum, and maximumum ΔV to deploy the satellites in these constellations are listed in Table I; these are calculated using the equations presented in [21], [22] and [23], assuming a low-thrust transfer of each satellite from ISS orbit to its target orbit. The RAAN-spread constellations are consistently easier to deploy than their MOG counterparts. The difference is smallest (approx. $10\,\mathrm{m\,s^{-1}}$) for 2-2-τ arrangements, and largest (approx. $60\,\mathrm{m\,s^{-1}}$) for g-3-τ arrangements.

The rest of the work considers constellation performance solely in terms of the quality metrics q_1 and q_2, assuming that they are properly deployed and maintained.

B. Constellation performance simulation

Orbits for the MOG and RAAN-spead RO constellations in Table I and for the GNSS constellations are simulated using Systems Tool Kit (STK). All 31 Global Positioning System (GPS) satellites, 25 Global Navigation Satellite System (GLONASS) satellites, 26 Galileo satellites, and 46 BeiDou satellites are included; these orbits are initialized with current (as of September 25, 2020) two-line element sets (TLEs) and propagated using the Simplified General Perturbations model (SGP4). The RO spacecraft orbits are propagated using the STK two-body propagator in order to simulate the effects of proper constellation maintenance, mainly the preservation of altitude and relative plane orientation; correspondingly, the slight apsidal-precession corrections to the MOG semi-major axes (see [19]) are removed. All occultation soundings—both rising and setting—during a six-month simulated flight starting on January 1, 2020 are recorded, subject to a 60° half-width boresight angle restriction. Soundings are grouped into clusters if they (1) all involve the same GNSS satellite, (2) each involve a unique receiver satellite, (3) all occur within half an hour, and (4) all occur within $3000\,\mathrm{km}$. The quality metrics q_1 and q_2 are calculated for each resulting cluster.

Figure 4 shows one day's worth of soundings for a 2-2-300 MOG and RAAN-spread constellation. The distribution of clusters is nearly identical for each constellation, as would be expected given the identical reference orbits and delay parameters. The MOG constellation shows consistent q_2 performance over all sampled latitudes, while the RAAN-spread constellation gives an increased concentration of high-q_2 clusters in the high latitudes. However, the performance does not consistently degrade; the RAAN-spread constellation still yields many low-q_2 clusters in the high latitudes.

Figure 5 shows a latitude-binned box plot of the q_1 and q_2 metrics for 2-2-300 MOG and RAAN-spread constellations over the full six-month period. The red and blue curves represent the log-mean quality metrics over the latitude range for the MOG and RAAN-spread constellations respectively. This confirms the principal observation from Fig. 4: the MOG constellation obtains uniform quality performance over all latitudes, while the cluster qualities of the RAAN-spread constellation degrade slightly toward the high latitudes. The RAAN-spread constellation performs slightly better than the MOGs in the equatorial regions.

The results for all considered constellations are summarized in Table II. Low latitudes ($|\phi| \leq 25^\circ$) are summarized in Table IIa, while mid latitudes ($25^\circ < |\phi| \leq 70^\circ$) are summarized in Table IIb. Due to the chosen reference inclination of 51.4°, no clusters were obtained in high latitudes ($|\phi| > 70^\circ$). For all considered constellations, the number of clusters in each latitude region is approximately equal, with a slight decrease noticeable as the delay τ is increased. This decrease is caused by long-delay constellations occasionally missing some occultation opportunities due to a change in GPS position over the delay time, for example if one group is able to catch an occultation which is no longer visible to the second group. Note that N_{occults} and N_{clusters} in Table II count the number of occultations and clusters, respectively; these are related by $N_{\text{occults}} \approx g \cdot m \cdot N_{\text{clusters}}$.

In both latitudinal regions, for all constellations, increasing the time delay τ between satellite groups improved the cluster quality metrics. Since q_2 decreases with increasing time delay, it can be inferred that the along-track cluster spacing due to the delayed groups is the limiting axis of uncertainty for wave vector reconstruction. However, the feasible delay between groups is limited by the time scale of the atmospheric features being observed. Larger constellations with equivalent time delays also demonstrated better performance in all regions; this is expected, since the number of samples in each cluster—and therefore the information—available for wave vector reconstruction increases with the number of satellites.

At mid latitudes, MOG constellations consistently outperform corresponding RAAN-spread constellations in both q_1 and q_2. This mid-latitude performance gap is illustrated for 2-2-300 constellations for q_1 and q_2 in Figures 5a and 5b, respectively. At low latitudes, disparities between the performance of equivalent MOG and RAAN-spread constellations are inconsistent, and such disparities are much smaller than those in mid-latitude regions. In this regime, nearly all RAAN-spread constellations perform slightly better in q_1 than MOGs, however only small RAAN-spread constellations (e.g. 2-2-τ arrangements) outperform their MOG counterparts in q_2.

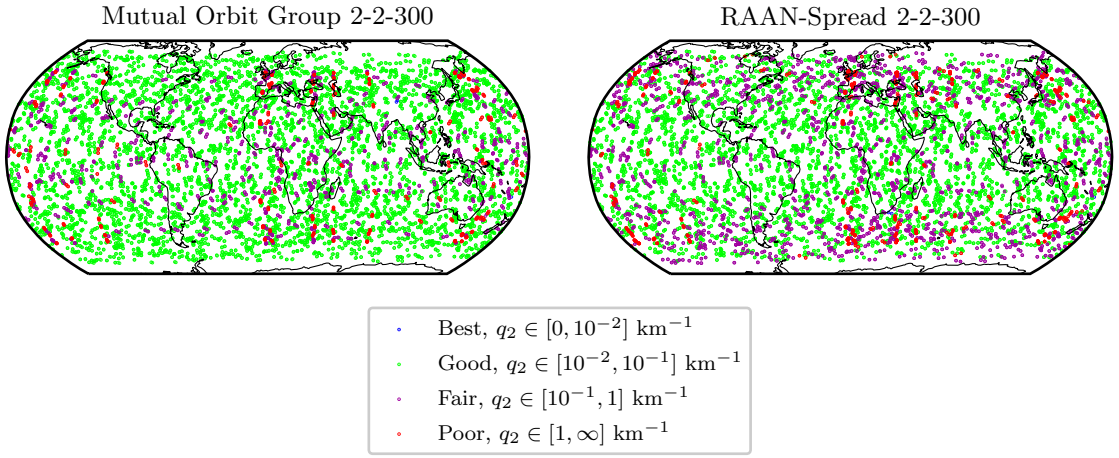

Fig. 4: One day of soundings from all GNSS constellations for a 2-2-300 MOG constellation (left) and a 2-2-300 RAAN-spead constellation (right), colored by q_2. Both constellations have good spatial coverage of the globe, with nearly identical cluster distributions. However, the RAAN-spread constellation gives more high-q_2 clusters in the higher latitudes, while the MOG constellation shows consistent quality performance. The *best* range roughly corresponds to reconstruction of a typical wave vector with less than 10% error.

TABLE II: Number of occultations (GPS, GLONASS, Galileo, and BeiDou), number of clusters, median cluster q_1, and median cluster q_2 over six simulated months for two latitude ranges. Lower q_1 and q_2 values indicate better performance.

(a) Summary of Sounding Clusters in Low Latitudes, $|\phi| \leq 25°$

	Mutual Orbit Group Constellation				RAAN-spread Constellation			
g-m-τ [s]	N_{occults}	N_{clusters}	mdn. q_1 [km^{-2}]	mdn. q_2 [km^{-1}]	N_{occults}	N_{clusters}	mdn. q_1 [km^{-2}]	mdn. q_2 [km^{-1}]
2-2-60	758235	188717	1.672×10^{-3}	6.910×10^{-2}	757556	188676	1.324×10^{-3}	6.273×10^{-2}
2-2-150	758417	187994	6.704×10^{-4}	5.107×10^{-2}	757720	187953	5.290×10^{-4}	4.573×10^{-2}
2-2-300	758530	186733	3.361×10^{-4}	4.784×10^{-2}	757721	186661	2.639×10^{-4}	4.266×10^{-2}
2-2-600	759044	184119	1.683×10^{-4}	4.663×10^{-2}	758121	184063	1.313×10^{-4}	4.143×10^{-2}
3-3-60	1706129	188214	4.540×10^{-4}	3.696×10^{-2}	1704521	188176	4.407×10^{-4}	3.866×10^{-2}
3-3-150	1706775	186705	1.806×10^{-4}	3.204×10^{-2}	1704775	186656	1.749×10^{-4}	3.473×10^{-2}
3-3-300	1707673	184112	8.813×10^{-5}	3.065×10^{-2}	1705432	184081	8.537×10^{-5}	3.354×10^{-2}
3-3-600	1710626	178738	3.640×10^{-5}	2.804×10^{-2}	1708409	178789	3.680×10^{-5}	2.983×10^{-2}
2-3-60	1137578	188774	1.113×10^{-3}	5.639×10^{-2}	1136363	188682	1.081×10^{-3}	5.572×10^{-2}
2-3-150	1137528	188002	4.451×10^{-4}	4.140×10^{-2}	1136564	187951	4.319×10^{-4}	4.469×10^{-2}
2-3-300	1179219	192940	1.798×10^{-4}	3.644×10^{-2}	1136579	186663	2.155×10^{-4}	4.223×10^{-2}
2-3-600	1138824	184158	1.108×10^{-4}	3.754×10^{-2}	1137311	184089	1.072×10^{-4}	4.131×10^{-2}
3-4-600	2280877	178669	2.729×10^{-5}	2.429×10^{-2}	2277732	178764	2.975×10^{-5}	2.781×10^{-2}

(b) Summary of Sounding Clusters in Mid Latitudes, $25° < |\phi| \leq 70°$

	Mutual Orbit Group Constellation				RAAN-spread Constellation			
g-m-τ [s]	N_{occults}	N_{clusters}	mdn. q_1 [km^{-2}]	mdn. q_2 [km^{-1}]	N_{occults}	N_{clusters}	mdn. q_1 [km^{-2}]	mdn. q_2 [km^{-1}]
2-2-60	1192011	296258	1.169×10^{-3}	4.804×10^{-2}	1192121	296284	2.265×10^{-3}	8.899×10^{-2}
2-2-150	1191922	294893	4.687×10^{-4}	4.126×10^{-2}	1191937	294887	9.069×10^{-4}	8.163×10^{-2}
2-2-300	1191742	292667	2.349×10^{-4}	4.093×10^{-2}	1191963	292655	4.536×10^{-4}	8.032×10^{-2}
2-2-600	1191227	288240	1.179×10^{-4}	4.120×10^{-2}	1191568	288201	2.270×10^{-4}	7.979×10^{-2}
3-3-60	2682007	295273	3.179×10^{-4}	2.817×10^{-2}	2682236	295374	7.551×10^{-4}	6.738×10^{-2}
3-3-150	2681506	292580	1.271×10^{-4}	2.708×10^{-2}	2681905	292653	3.011×10^{-4}	6.545×10^{-2}
3-3-300	2680437	288141	6.328×10^{-5}	2.672×10^{-2}	2681278	288186	1.409×10^{-4}	6.307×10^{-2}
3-3-600	2677675	279468	3.037×10^{-5}	2.481×10^{-2}	2678382	279434	5.348×10^{-5}	4.340×10^{-2}
2-3-60	1787863	296126	7.782×10^{-4}	3.919×10^{-2}	1788134	296278	1.850×10^{-3}	8.636×10^{-2}
2-3-150	1787892	294791	3.116×10^{-4}	3.356×10^{-2}	1787937	294889	7.405×10^{-4}	8.111×10^{-2}
2-3-300	1758931	287938	1.424×10^{-4}	3.286×10^{-2}	1787911	292655	3.703×10^{-4}	8.020×10^{-2}
2-3-600	1786628	288135	7.802×10^{-5}	3.304×10^{-2}	1787220	288196	1.853×10^{-4}	7.974×10^{-2}
3-4-600	3570141	279375	2.278×10^{-5}	2.149×10^{-2}	3571345	279448	4.286×10^{-5}	4.070×10^{-2}

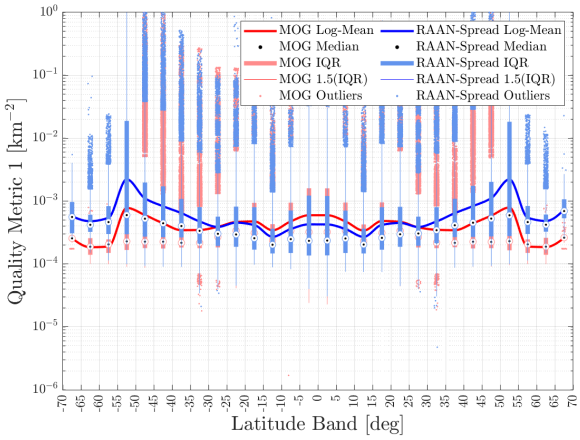

(a) q_1 for MOG (red) and RAAN-spread (blue) 2-2-300

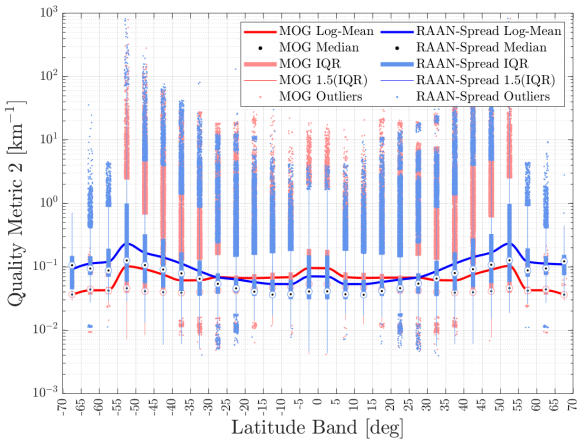

(b) q_2 for MOG (red) and RAAN-spread (blue) 2-2-300

Fig. 5: q_1 and q_2 over latitude for 2-2-300 constellations. The RAAN-spread constellation performs slightly better than the MOG at low latitudes, but noticeably worse in the mid latitudes.

V. Analysis of RO Quality Distribution

This section provides an explanation and intuition for the distribution of clusters and cluster qualities, in both the MOG and RAAN-spread cases. The analysis focuses on q_2, the metric representing the worst axis of wave-vector uncertainty. Low q_2 provides a more meaningful guarantee of tomographic performance, as the resulting cluster will be able to resolve a wave-vector in any direction. Additionally, spread of a cluster in one horizontal direction tends to be dominated by GNSS satellite motion and Earth rotation over the chosen delay time regardless of constellation geometry. Focusing on the worst case axis provides an illuminating distinction about where constellation arrangement results in favorable or unfavorable cluster geometry.

Information about the relative positions of the GNSS and RO spacecraft is given by the ray path azimuth α, which is defined as the angle between the occultation ray-path and the local northward direction at the point of tangency. Positive angles indicate a southwest–northeast ray, and negative

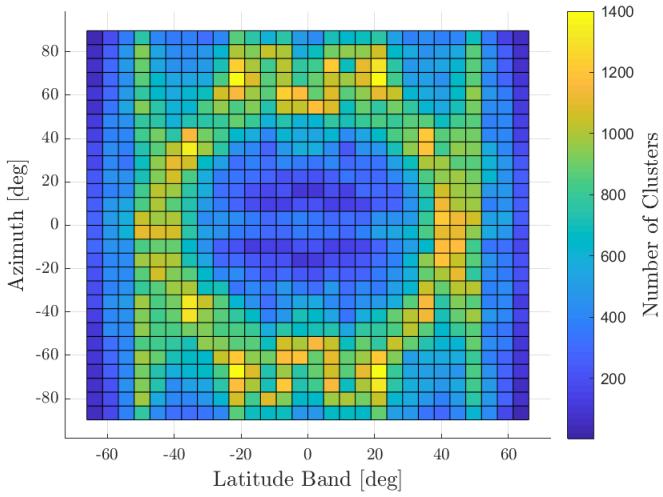

Fig. 6: Cluster density for a 2-2-300 MOG constellation over all possible latitudes and ray azimuths for a six-month simulation of 2-2-300 MOGs. Azimuth is defined at the point of tangency as the angle clockwise from the local northward vector to the transmitter-receiver line. The corresponding plot for the RAAN-spread constellation is nearly identical, since the location and ray-path geometry of soundings is dependent only on the reference orbit and delay parameter.

indicate northwest–southeast. Examining the distribution of quality metrics as a function of latitude and ray path azimuth illuminates the underlying structure of the constellation quality distributions resulting from unavoidable scenario geometry.

Figure 6 shows the number of clusters observed over the six-month 2-2-300 MOG simulation in each 5°-by-5° bin of latitude and ray azimuth. The equivalent RAAN-spread figure is identical. It can be seen that there is a significant concentration of clusters falling on an ellipse; most clusters in the equatorial regions tend to have nearly east-west ray paths with $|\alpha| \approx 60°$–$70°$, while clusters in the higher latitudes (especially near $|\phi| \approx 45°$–$50°$) tend to have north–south ray paths. There are significant clusters occurring near 20° latitude, with high azimuth. The increased occurrence of soundings at particular latitudes agrees with the singularities in sounding density predicted by [24]; these singularities come about due to the inclination of GNSS constellations, and different GNSS constellations have different singularities.

Figure 7 shows the same distribution as shown in Fig. 6, but partitioned by cluster q_2 value. Figures 7(a,c,e,g) show four increasing q_2 ranges for the MOG constellation, while Figs. 7(b,d,f,h) show the same for the RAAN-spread constellation. Although the overall distribution of clusters for each constellation is the same (per Figure 6), the quality breakdown differs significantly. The first range for the MOG distribution (a) shows the significant concentration of the best clusters into bands at $\phi \approx \pm 35°$, while the second range (c) shows that good clusters have a latitude-azimuth structure which closely matches the overall distribution shown in Fig. 7. Fair clusters (e) and poor clusters (g) are approximately uniform in distribution, but poor clusters (g) have additional

concentrations at the end of the latitude range. The first range of the RAAN-spread distribution (b) shows that the best clusters are focused near the equator, with some spread in the low latitudes. The second range (d) shows that good clusters are slightly focused in the low latitudes, but in general have good spread. The third range (f) shows the concentration of fair clusters into the high latitudes, while the fourth range (h) shows the relative lack of poor clusters as compared to the MOG constellation.

Figure 8 shows the same latitude/azimuth/q_2 data as Fig. 7, but as a scatter-plot colored by q_2 value. The left view in each of Figs. 8a and 8b show the distribution with low-q_2 clusters on top of the view (such that each latitude/azimuth point is colored per the best observed cluster at that location), while the right views show the same data with high-q_2 clusters on top of the view (such that each point is colored per the worst observed cluster at that location). It can be seen on the left that, for both constellation types, there are good clusters observed at almost all latitudes. For the RAAN-spread constellation, however, the edges of the latitude range show a decay toward high-q_2 clusters. The structure observed on the right indicates that many of the worst-performing clusters follow from geometric limitations of occultation geometry present for both constellations. Where this structure terminates just above $\pm 50^\circ$ latitude, the right MOG scatterplot (a) reveals the edges of the underlying mat of consistent low-q_2 clusters; the right RAAN-spread scatterplot (b) shows high-latitude clusters exhibit poor worst-case performance even past the edge of this structure.

Overall, Figs. 7 and 8 support the following explanation for the latitude-dependent trends observed in Figure 5b: Both the MOG and RAAN-spread constellations exhibit poor outlier cluster performance when limited by occultation geometry (as is the case frequently in the low and lower-mid latitudes). However, the MOG constellations otherwise exhibit good cluster quality consistently over the latitude range, while the RAAN-spread constellations exhibit slightly improved equatorial quality trending toward significantly reduced quality at the edge of the latitude range.

VI. Conclusions

Radio occultation (RO) receivers that leverage the transmitters of the Global Navigation Satellite Systems (GNSS) are a powerful tool for making remote atmospheric measurements around the globe. In general, the wide spatial and temporal distribution of these measurements is a desirable feature, but it makes study of short-lived, small-scale features difficult or impossible. However, careful arrangement of the RO spacecraft into close-flying groups can cluster the RO measurements in both space and time, providing multiple soundings of localized phenomena. Specifically, the horizontal wave vectors of any internal gravity waves present can be inferred via tomography. In order to consistently reconstruct wave vectors, the sounding clusters must have a two-dimensional distribution on the ground. String-of-pearls constellations tend to produce soundings along a line, and are therefore insufficient for this task.

This paper first introduces two quality metrics q_1 and q_2 which predict the tomographic performance (wave vector reconstruction error) of a sounding cluster. q_1 and q_2 are used to assess the expected performance of two alternative RO constellation types, the mutual orbit group (MOG) and RAAN-spread formations. For either design an increased number of satellites and a longer spacing between groups produces more high-quality clusters on average; however, the number of spacecraft is obviously limited by budget and other practicalities, while the group spacing delay is limited by the time scale of the features we seek to observe (a few tens of minutes for internal gravity waves; see Fig. 8(b) of [6]). For a fixed delay and number of spacecraft, the choice between a MOG or RAAN-spread constellation depends on the propulsion available and the desired performance at low and high latitudes. MOG constellations require consistent propulsion expenditure (using ΔV on the order of 2–3 $\mathrm{m\,s^{-1}\,day^{-1}}$ for the considered constellation parameters) to counteract differential nodal regression, while the RAAN-spread design avoids this problem. At the cost of this ΔV, MOG constellations yield a more-even distribution of high-quality clusters in all sampled latitudes. In comparison, RAAN-spread constellations exhibit slightly higher quality in the equatorial regions but trend to consistently-reduced quality at high latitudes for the considered inclination of 51.4°.

Finally, this paper explores the causes of the quality distributions observed by examining the distributions in latitude and ray path azimuth. All soundings show a latitude-azimuth relationship dictated by the geometry of the constellation reference orbit and the GNSS constellations. It is shown that many of the poorest- and best-performing clusters for both constellation types were outliers resulting from the geometric structure of RO soundings themselves. For MOG constellations, the best clusters tend to lie in bands at about $\pm 35^\circ$ latitude, and the worst at $\pm 55^\circ$; typical clusters are evenly distributed, and exhibit good performance. For RAAN-spread constellations, the best clusters result from east–west soundings at the equator, and clusters follow a consistent trend of decreasing in quality with increasing latitude and decreasing azimuth; poor-performing outlier clusters are not as common as in the MOG case.

This work, therefore, suggests the following principle for deciding between mutual orbit group and RAAN-spread RO tomography constellations: unless high-ΔV-capacity propulsion is available and high-quality soundings at high latitudes are specifically desired, RAAN-spread constellations should be used. Such constellations consistently achieve equivalent or better wave vector reconstruction at low latitudes, where most emission of gravity waves from tropospheric deep convection occurs and where gravity waves—in part—drive the quasi-biennial oscillation. Additionally, over their increased lifetime, such constellations yield more reconstructions of high quality even in the mid and high latitudes. These insights will inform the constellation design necessary for future work in this sequence of papers on the development and potential performance of a nano-satellite gravity wave observatory.

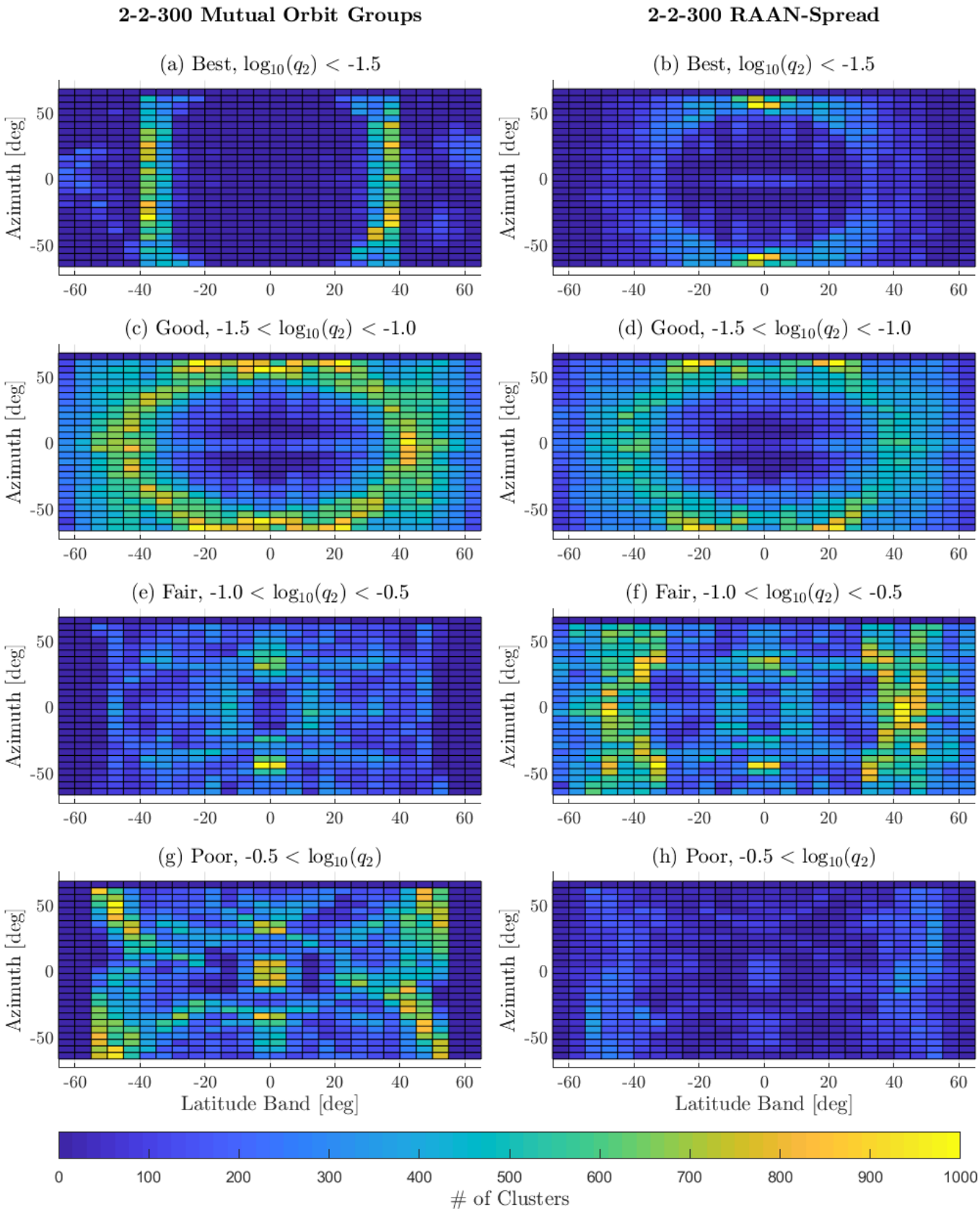

Fig. 7: The 2-2-300 latitude-azimuth cluster distribution shown in Fig. 6, partitioned into bins by cluster q_2 quality. Subfigures (a,c,e,g) correspond to four increasing q_2 ranges for a MOG constellation, while subfigures (b,d,f,h) correspond to the same ranges for the corresponding RAAN-spread constellation.

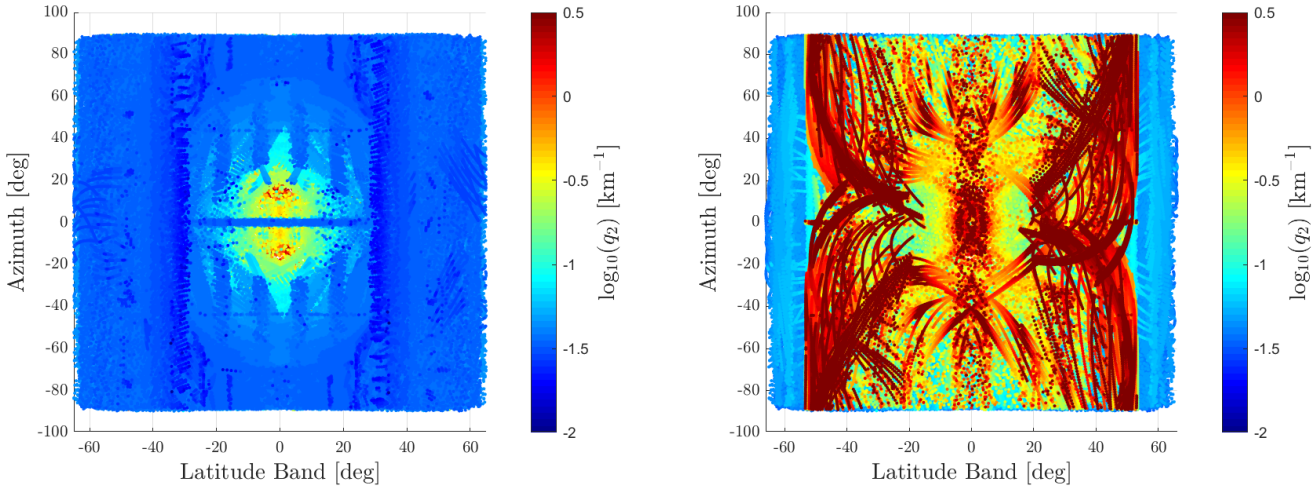

(a) Mutual Orbit Groups, 2-2-300. On the left, note the even presence of good, low-q_2 clusters at all latitudes and most azimuths. Bad, high-q_2 clusters (right) due to poor geometry are present only inside the range of approximately $(-52^\circ, 52^\circ)$, and seem to follow a latitude-azimuth structure.

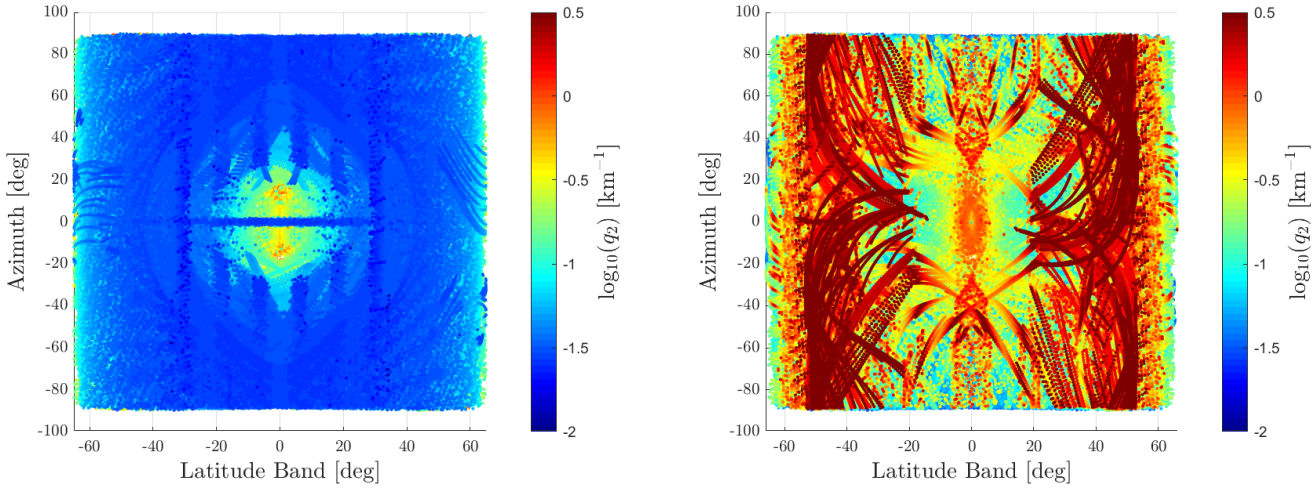

(b) RAAN-Spread, 2-2-300. On the left, note the consistent presence of good, low-q_2 clusters at most latitudes, except at the edges of the range. Bad, high-q_2 clusters (right) are now present all the way to the edge of the latitude range, extending past the edge of the latitude-azimuth structure.

Fig. 8: Six months of occultation clusters for MOG and RAAN-spread 2-2-300 constellations, plotted against latitude and azimuth, and colored by q_2. Left shows the data with lowest-q_2 (best) clusters plotted on top, right shows the same data with the highest-q_2 (worst) clusters on top.

ACKNOWLEDGMENTS

We acknowledge Analytical Graphics, Inc. for use of the Systems Tool Kit (STK) and the U.S. National Aeronautics and Space Administration for use of the General Mission Analysis Tool (GMAT). STK was used under a purchased license and GMAT under an open license. S. Leroy, L. Halperin, and A. Gagnon were supported by grant ATM-1850276 of the National Science Foundation.

REFERENCES

[1] D. Fritts and M. Alexander, "Gravity wave dynamics and effects in the middle atmosphere," *Rev. Geophys.*, vol. 41, no. 1, p. doi:10.1029/2001RG000106, 2003.

[2] R. Lindzen and J. Holton, "A theory of the quasi-biennial oscillation," *J. Atmos. Sci.*, vol. 25, no. 6, pp. 1095–1107, 1968.

[3] M. P. Baldwin, L. J. Gray, T. J. Dunkerton, K. Hamilton, P. H. Haynes, W. J. Randel, J. R. Holton, M. J. Alexander, I. Hirota, T. Horinouchi, D. Jones, J. Kinnersley, C. Marquardt, K. Sato, and M. Takahashi, "The quasi-biennial oscillation," *Rev. Geophys.*, vol. 39, no. 2, pp. 179–229, 2001.

[4] G. Mastrantonio, F. Einaudi, D. Fua, and D. Lalas, "Generation of gravity waves by jet streams in the atmosphere," *J. Atmos. Sci.*, vol. 33, pp. 1730–1738, 1977.

[5] J. Holton, P. Haynes, M. McIntyre, A. Douglass, R. Rood, and L. Pfister, "Stratosphere-troposphere exchange," *Rev. Geophys.*, vol. 33, no. 4, pp. 403–439, 1995.

[6] M. Alexander, M. Geller, C. McLandress, S. Polavarapu, P. Preusse, F. Sassi, K. Sato, S. Eckermann, M. Ern, A. Hertzog, Y. Kawatani, M. Pulido, T. Shaw, M. Sigmond, R. Vincent, and S. Watanabe, "Review article: Recent developments in gravity-wave effects in climate models and the global distribution of gravity-wave momentum flux from observations and models," *Q. J. R. Meteorol. Soc.*, vol. 136, pp. 1103–1124, 2010.

[7] E. Kursinski, G. Hajj, J. Schofield, R. Linfield, and K. Hardy, "Observing Earth's atmosphere with radio occultation measurements using the Global Positioning System," *J. Geophys. Res.*, vol. 102, no. D19, pp. 23 429–23 465, 1997.

[8] G. Hajj, E. Kursinski, L. Romans, W. Bertiger, and S. Leroy, "A technical description of atmospheric sounding by GPS occultation," *J. Atmos. Solar Terr. Phys.*, vol. 64, no. 4, pp. 451–469, 2002.

[9] M. E. Gorbunov, H.-H. Benzon, A. S. Jensen, M. S. Lohmann, and A. S. Nielsen, "Comparative analysis of radio occultation processing approaches based on fourier integral operators," *Radio Science*, vol. 39, no. 6, 2004. [Online]. Available: https://agupubs.onlinelibrary.wiley.com/doi/abs/10.1029/2003RS002916

[10] L. Hoffmann and M. Alexander, "Retrieval of stratospheric temperatures from Atmospheric Infrared Sounder radiance measurements for gravity waves studies," *J. Geophys. Res.*, vol. 114, p. doi:10.1029/2008JD011241, 2009.

[11] ——, "Occurrence frequency of convective gravity waves during the North American thunderstorm season," *J. Geophys. Res.*, vol. 115, p. doi:10.1029/2010JD014401, 2010.

[12] L. Hoffmann, X. Xue, and M. Alexander, "A global view of stratospheric gravity wave hotspots located with Atmospheric Infrared Sounder observations," *J. Geophys. Res.*, vol. 118, p. doi:10.1029/2012JD018658, 2010.

[13] V. N. Gubenko, A. G. Pavelyev, and V. E. Andreev, "Determination of the intrinsic frequency and other wave parameters from a single vertical temperature or density profile measurement," *Journal of Geophysical Research: Atmospheres*, vol. 113, no. D8, 2008. [Online]. Available: https://agupubs.onlinelibrary.wiley.com/doi/abs/10.1029/2007JD008920

[14] V. N. Gubenko, A. G. Pavelyev, R. R. Salimzyanov, and A. A. Pavelyev, "Reconstruction of internal gravity wave parameters from radio occultation retrievals of vertical temperature profiles in the earth's atmosphere," *Atmospheric Measurement Techniques*, vol. 4, no. 10, pp. 2153–2162, 2011. [Online]. Available: https://amt.copernicus.org/articles/4/2153/2011/

[15] K. Cahoy, L. P. Dyrud, J. T. Fentzke, R. L. Bishop, P. R. Straus, G. Lightsey, T. E. Humphreys, T. Meehan, and A. J. Mannucci, "Small and Low-Cost GNSS Radio Occultation Receivers," in *AGU Fall Meeting Abstracts*, vol. 2011, Dec. 2011, pp. SA24A–08.

[16] V. Nguyen, T. Duly, D. Ector, V. Irisov, O. Nogues-Correig, L. Tan, and T. Yuasa, "Spire's 3U CubeSat GNSS-RO Constellation for Meteorological and Space Weather Applications," in *AGU Fall Meeting Abstracts*, vol. 2017, Dec. 2017, pp. A33M–06.

[17] L. Wang and M. Alexander, "Global estimates of gravity wave parameters from GPS radio occultation temperature data," *J. Geophys. Res.*, vol. 115, p. doi:10.1029/2010JD013860, 2010.

[18] T. Schmidt, P. Alexander, and A. de la Torre, "Stratospheric gravity wave momentum flux from radio occultations," *J. Geophys. Res.*, vol. 121, p. doi:10.1002/2015JD024135, 2016.

[19] S. Leroy, R. Fitzgerald, K. Cahoy, J. Abel, and J. Clark, "Orbital maintenance of a constellation of CubeSats for internal gravity wave tomography," *IEEE J. Sel. Topics in Appl. Earth Obs. and Remote Sens.*, vol. 13, pp. 307–407, 2020.

[20] S. Leroy and A. Ingersoll, "Radio scintillations in Venus's atmosphere: Application of a theory of gravity wave generation," *J. Atmos. Sci.*, vol. 53, no. 7, pp. 1018–1028, 1996.

[21] M. Martinez-Sanchez and P. Lozano. (Spring 2015) 16.522 Space Propulsion. Massachusetts Institute of Technology: MIT OpenCourseWare. [Online]. Available: https://ocw.mit.edu

[22] A. Ruggiero, P. Pergola, S. Marcuccio, and M. Andrenucci, "Low-Thrust Maneuvers for the Efficient Correction of Orbital Elements," in *32nd International Electric Propulsion Conference*, 2011, pp. 1–13.

[23] C. R. McInnes, "Low-Thrust Orbit Raising With Coupled Plane Change and J2 Precession," *Journal of Guidance, Control, and Dynamics*, vol. 20, no. 3, pp. 607–609, 1997.

[24] S. Leroy, C. Ao, and O. Verkhoglyadova, "Mapping GPS radio occultation data by Bayesian interpolation," *J. Atmos. Ocean. Tech.*, vol. 29, pp. 1062–1074, 2012.

Riley Fitzgerald is currently a Ph.D. student in the Department of Aeronautics and Astronautics at the Massachusetts Institute of Technology, where he works with the Space Telecommunications, Astronomy, and Radiation (STAR) Laboratory as a Draper Fellow. His research is primarily in orbital mechanics and spacecraft navigation. He holds an M.S. in Aeronautics and Astronautics from M.I.T. (2018), and a B.S.E. in Mechanical and Aerospace Engineering from Princeton University (2016).

Lucy Halperin is currently a Masters student in the Department of Aeronautics and Astronautics at the Massachusetts Institute of Technology. She works in the Space, Telecommunications, Astronomy, and Radiation (STAR) Laboratory with Professor Kerri Cahoy. Her research is primarily in the applications of machine learning to small satellite formation flying and telemetry analysis. She holds a B.S. in Aerospace Engineering from M.I.T. (2019).

Stephen Leroy is currently a Principal Scientist at Atmospheric and Environmental Research, Inc. He obtained a B.A. in Physics (1988) from Cornell University and a M.Sc. (1990) and Ph.D. (1994) in Planetary Science from the California Institute of Technology. His previous positions were as a Scientist at the NASA Jet Propulsion Laboratory (1994–2004) and as a Project Scientist in Prof. James Anderson's group at Harvard University (2004–2017). His research has covered atmospheric internal gravity waves, GNSS radio occultation, nadir spectral infrared sounding, detection and attribution of climate change, and Bayesian information theory applied to remote sensing data types.

Amelia Gagnon is currently a Masters student in the Department of Aeronautics and Astronautics at the Massachusetts Institute of Technology. She works in the Space, Telecommunications, Astronomy, and Radiation (STAR) Laboratory with Professor Kerri Cahoy. Her primary research is in constellations of Earth-observing satellites. She holds a B.S. in Electrical Engineering from the University of North Dakota (2015).

Kerri Cahoy is an Associate Professor of Aeronautics and Astronautics at MIT and leads the Space Telecommunications, Astronomy, and Radiation (STAR) Laboratory. Dr. Cahoy received a B.S. (2000) in Electrical Engineering from Cornell University, and M.S. (2002) and Ph.D. (2008) in Electrical Engineering from Stanford University. Dr. Cahoy previously worked at Space Systems Loral, as a postdoctoral fellow at NASA Ames, and currently leads nanosatellite atmospheric sensing, optical communications, and exoplanet technology demonstration missions.

James Clark is currently a post-doctoral researcher in the Department of Aeronautics and Astronautics at the Massachusetts Institute of Technology. His research is primarily in laser communication, mission and trajectory design, and advanced concept development. He holds an S.B. (2014), an S.M. (2016), and a Ph.D. (2020) in Aeronautics and Astronautics from M.I.T.